

# **Kinetics of optical properties of human colorectal tissues during optical clearing: a comparative study between normal and pathological tissues**

Isa Carneiro  
Sónia Carvalho  
Vânia Silva  
Rui Henrique  
Luís Oliveira  
Valery V. Tuchin

# Kinetics of optical properties of human colorectal tissues during optical clearing: a comparative study between normal and pathological tissues

Isa Carneiro,<sup>a</sup> Sónia Carvalho,<sup>a</sup> Vânia Silva,<sup>b</sup> Rui Henrique,<sup>a,c</sup> Luís Oliveira,<sup>b,d,\*†</sup> and Valery V. Tuchin<sup>e,f,g,†</sup>

<sup>a</sup>Portuguese Oncology Institute of Porto, Department of Pathology and Cancer Biology and Epigenetics Group-Research Centre, Porto, Portugal

<sup>b</sup>Polytechnic of Porto, School of Engineering, Centre of Innovation in Engineering and Industrial Technology, Porto, Portugal

<sup>c</sup>University of Porto, Institute of Biomedical Sciences Abel Salazar, Department of Pathology and Molecular Immunology, Porto, Portugal

<sup>d</sup>Polytechnic of Porto, School of Engineering, Physics Department, Porto, Portugal

<sup>e</sup>Saratov State University, Research-Educational Institute of Optics and Biophotonics, Saratov, Russia

<sup>f</sup>Institute of Precision Mechanics and Control of the Russian Academy of Sciences, Laboratory of Laser Diagnostics of Technical and Living Systems, Saratov, Russia

<sup>g</sup>Tomsk State University, Interdisciplinary Laboratory of Biophotonics, Tomsk, Russia

**Abstract.** To characterize the optical clearing treatments in human colorectal tissues and possibly to differentiate between treatments of normal and pathological tissues, we have used a simple indirect method derived from Mie scattering theory to estimate the kinetics of the reduced scattering coefficient. A complementary method to estimate the kinetics of the scattering coefficient is also used so that the kinetics of the anisotropy factor and of the refractive index are also calculated. Both methods rely only on the thickness and collimated transmittance measurements made during treatment. The results indicate the expected time dependencies for the optical properties of both tissues: an increase in the refractive index and anisotropy factor and a decrease in the scattering coefficients. The similarity in the kinetics obtained for normal and pathological tissues indicates that optical clearing treatments can be applied also in pathological tissues to produce similar effects. The estimated time dependencies using experimental spectral data in the range from 400 to 1000 nm allowed us to compare the kinetics of the optical properties between different wavelengths. © 2018 Society of Photo-Optical Instrumentation Engineers (SPIE) [DOI: 10.1117/1.JBO.23.12.121620]

Keywords: optical clearing; optical properties control; refractive index matching; kinetics of optical properties; colorectal tissues; adenocarcinoma.

Paper 180354SSRR received Jun. 14, 2018; accepted for publication Nov. 14, 2018; published online Dec. 6, 2018.

## 1 Introduction

The authors would like to congratulate Professor Jacques for his 70th jubilee. Professor Jacques was one of the pioneers in tissue optics and biophotonics, who contributed with many reference papers in this field. Several of those papers were and still are used today by many scientists as reference works for their research. We are some of those researchers who look into Professor Jacques's papers when some questions arise.

The relative refractive index (RI) of biological tissues, which is commonly used to characterize scattering efficiency, is a parameter that depends on the RI of the interstitial fluid (ISF) ( $\bar{n}_0$ ) and on the RI of tissue scatterers ( $n_s$ ):<sup>1</sup>

$$m = \frac{n_s}{\bar{n}_0}. \quad (1)$$

As most biological tissues have  $m > 1$ , high and multiple light scattering will occur.<sup>1</sup> According to the Mie scattering theory, the reduced scattering coefficient ( $\mu'_s$ ) can be defined as a function of  $m$ ,  $\bar{n}_0$ , light wavelength ( $\lambda$ ), the mean scatterer radius ( $a$ ), and the volume density of the scattering centers ( $\rho_s$ ):<sup>2,3</sup>

$$\mu'_s = 3.28\pi a^2 \rho_s \left( \frac{2\pi \bar{n}_0 a}{\lambda} \right)^{0.37} (m - 1)^{2.09}. \quad (2)$$

Equation (2) was validated by the authors of Ref. 3 for the visible-near infrared (NIR) spectral range and for a system of noninteracting spherical particles with a mean diameter of  $2a$  and when scattering anisotropy factor  $g > 0.9$ ,  $5 < 2\pi a/\lambda < 50$ , and  $1 < m < 1.1$ . Testing of Eq. (2) outside these limits has not been reported.

For a tissue to become completely transparent,  $m$  should reduce to 1 and  $\mu'_s$  should decrease to zero. One way to reduce light scattering in biological tissues is to use the optical clearing (OC) immersion method, which was proposed two decades ago.<sup>4</sup> Since then, a wide range of techniques has been used to evaluate its efficiency in various tissues.<sup>1,5,6</sup> This method has high potential to be applied in clinical practice as the temporary transparency effect created by optical clearing agents (OCAs) increases light transmittance in tissues through the reduction in light scattering.<sup>7</sup> As already demonstrated, the main mechanisms of OC treatments are tissue dehydration and RI matching,<sup>8</sup> which reduce tissue scattering through the partial replacement of interstitial water by an OCA with higher RI, better matched to one or to a few types of tissue scatterers.<sup>9</sup> As results of these treatments, increased light penetration depth,

\*Address all correspondence to Luís Oliveira, E-mail: lmo@isep.ipp.pt

†Authors contributed equally to this work.

increased fluorescence transport, or increased image contrast from deeper tissue layers are obtained.<sup>6,10–11</sup>

The water flux out of the tissue creates the dehydration mechanism and the OCA flux into the tissue provides the RI matching mechanism,<sup>8</sup> meaning that it is important to know the total water content of the tissue and if all water is able to move out. Biological tissues are known to have four states of water inside: strongly bound, tightly bound, weakly bound, and free water; only the last two (designated hereafter as mobile water) participate in the dehydration mechanism during short-term OC treatments.<sup>12</sup> Such mobile water can be found both in the ISF and inside tissue cells. To move it through cell membranes into the ISF, a strong osmotic pressure is necessary. In short-term OC treatments, total transparency cannot be obtained as strongly bound water is powerfully connected to tissue cells, organelles, and other tissue components.<sup>13</sup> Recent research has been presented, where strong OC stimulation was applied to make entire organs completely transparent.<sup>14,15</sup> For strongly and tightly bound water to convert into mobile water and flow out of the tissue, a strong long-term stimulation is also necessary.<sup>8</sup> In short-term OC treatments made with low osmotic strength OCAs, only the mobile water in the ISF will flow out.<sup>9</sup>

Considering the skin as an example tissue, the less-concentrated water types at all skin depths, for intact and OCA-treated skin, are the unbound and tightly bound water types (<10%), while the strongly bound and weakly bound water types represent the remaining >90%.<sup>12,16,17</sup> During OC treatments, changes in collagen hydration at the dermis depend on the OCA used. Skin tissues treated with glycerol suffer stronger effect than when treated with Omnipaque<sup>TM</sup><sup>18</sup> as bound water converts into free water due to an increased osmotic pressure caused by glycerol application.<sup>19,20</sup> Bound water can also convert into free water due to mechanical pressure,<sup>21,22</sup> and both the osmotic and mechanical pressures can lead to local skin dehydration.<sup>16</sup> During OC treatments, it is also important to consider the diffusion rate of the OCA into the tissue, which can be conditioned by the water flowing out. Weight, thickness, and collimated transmittance ( $T_c$ ) measurements made during treatments can be used to evaluate the diffusion properties of OCAs.<sup>19,23–26</sup>

Considering OCA diffusion into the skin, Omnipaque<sup>TM</sup> presents a much lower diffusion rate in skin than glycerol as its molar mass is 10 times higher than the molar mass of glycerol (821 and 92 g/mol, respectively).<sup>16</sup> When glycerol molecules penetrate into the skin, they bound water molecules, leading to a mixed flux between OCA-bound water going in and skin's water going out. We have previously showed<sup>27</sup> that the water content in the treating solutions has a high impact on the water flux out during treatment. Water flux out is minimal or even zero when the water in the treating solution matches the potentially mobile water in the tissue.<sup>28</sup> In these balanced conditions, only glycerol or iohexol molecules are flowing into the skin.<sup>16,19</sup> For unique glycerol diffusion into skin (solutions with 60% to 70% glycerol concentrations), glycerol presents the lowest diffusion coefficient in skin.<sup>28</sup> It has been demonstrated that mobile water [ $\sim$ 55% of total water in the skin (0 to 200  $\mu$ m)] is included in the water flux out from the skin during OC. Strongly bound water [ $\sim$ 44% of total water in the skin (0 to 200  $\mu$ m)] may also take part in the dehydration mechanism but with lower mobility.<sup>16</sup> Similar results have been obtained for skin,<sup>28</sup> and slightly higher values were obtained for mucosal

and muscle tissues.<sup>19,29</sup> Such difference can be explained by the skin heterogeneity and different water-bonding properties of epidermis and dermis in comparison with other tissues.

When an *ex vivo* slab-form tissue is immersed for a time period in a solution containing an OCA, treatment duration, OCA molecular structure, and osmolarity condition created transparency.<sup>8,23</sup> The partial and dynamic exchanges of the mobile water by the OCA create continuous changes in tissue's optical properties according to reported optical measurements.<sup>19,23,24</sup>

The literature indicates that during OC treatments, a reduction in the scattering coefficient ( $\mu_s$ ) and an increase in the anisotropy factor ( $g$ ) are expected.<sup>1</sup> To demonstrate that such variations occur, optical and thickness measurements made from a tissue under OC treatment can be used to estimate the time dependencies for the optical properties.

With the objective of testing Eq. (2) outside the limits where it was validated and to confirm the predictions of decreasing  $\mu_s$  (and  $\mu_s'$ ) and increasing  $g$  during OC treatments, we performed the research presented in the following sections. We used previous thickness and  $T_c$  kinetics measurements,<sup>19</sup> performed from human normal and pathological colorectal mucosa under treatment with glucose–water solutions to estimate the kinetics for the optical properties of these tissues. Such estimated time dependencies show how the optical properties evolve during treatment and allow one to identify and select treatment duration to obtain a desired decrease in  $\mu_s$  or increase in  $g$ . By comparing between the time dependencies of the optical properties of both tissues, we can see if differentiated response to the OC treatments is obtained for normal and pathological tissues.

## 2 Material and Methods

To conduct the present research, we have used normal and pathological colorectal tissues from human species. Section 2.1 presents tissue OC concept. Section 2.2 describes the collection and preparation of the biological tissues, and the evaluation of the total water content is given in Sec. 2.3. Thickness and  $T_c$  measurements were obtained in a previous study,<sup>19</sup> during treatments with glucose–water solutions and a brief description of these measurements is presented in Sec. 2.4. The reconstruction of natural  $\mu_s'(\lambda)$  is described in Sec. 2.5, and the calculation procedure to obtain the kinetics for  $\mu_s(\lambda)$ ,  $\bar{n}_0(\lambda)$ , and  $n_{\text{tissue}}(\lambda)$  is presented in Sec. 2.6. Section 2.7 describes the calculation of the time dependencies for  $\mu_s'(\lambda, t)$  and  $g(\lambda, t)$ . All the calculations consider a wavelength range between 400 and 1000 nm.

### 2.1 Tissue Optical Clearing Concept

During short-time OC treatments, the physical dimensions of tissue scatterers [scatterer radius  $a$ , in Eq. (1)] and their RI ( $n_s$ ) are not expected to change. Consequently, as the partial replacement of interstitial water by the OCA will produce some volume changes in the sample,  $\rho_s$  will suffer a variation. For a slab-form sample that has a small thickness relative to its superficial area, the time dependence of  $\rho_s$  [or scatterer volume fraction– $f_s(t)$ ] can be calculated from the time dependence of sample thickness [ $d(t)$ ]. By replacing  $\rho_s$  by  $f_s(t)$  in Eq. (1), the time dependence for  $\mu_s'$  can be calculated, provided that we can obtain the time dependence for  $\bar{n}_0$ .

If total and mobile water contents in the natural tissue are known, the variation of  $\bar{n}_0$  can be calculated during treatment according to Eq. (3):<sup>30</sup>

$$\bar{n}_0(t) = \frac{n_s}{\left[ \sqrt{\frac{\mu_s(t) \times d(t)}{\mu_s(t=0) \times d(t=0)}} \times \left( \frac{n_s}{n_0(t=0)} - 1 \right) + 1 \right]}, \quad (3)$$

where  $n_0(t=0)$  is the RI of the ISF for natural tissue;  $\mu_s(t=0)$  and  $\mu_s(t)$  are the scattering coefficients of the untreated tissue and during treatment, respectively; and  $d(t=0)$  and  $d(t)$  are the sample thicknesses of the untreated tissue and during treatment. If the optical properties of the untreated tissue are known, and considering that the absorption coefficient ( $\mu_a$ ) remains unchanged during treatment, the values of  $\mu_s(t=0)$  and  $\mu_s(t)$  can be calculated through Beer-Lambert equation for a particular wavelength:<sup>29,30</sup>

$$\mu_s(\lambda, t) = -\frac{\ln[T_c(\lambda, t)]}{d(t)} - \mu_a(\lambda). \quad (4)$$

As  $\mu_s$  is in general much higher than  $\mu_a$  in biological tissues, it is reasonable to neglect the variations of  $\mu_a$  during OC. Once the time dependence of  $\bar{n}_0$  is obtained, the time dependence of the RI of the total tissue [ $n_{\text{tissue}}(t)$ ] can be calculated with Gladstone and Dale equation:<sup>1,29-34</sup>

$$\begin{aligned} n_{\text{tissue}}(t) &= \bar{n}_0(t)f_0(t) + n_s f_s(t) \\ f_0(t) + f_s(t) &= 1, \end{aligned} \quad (5)$$

where  $f_0(t)$  is the time dependency for the volume fraction of the ISF. If spectral data are available, Eqs. (1)–(5) can be used to calculate the time dependencies for a wavelength range.

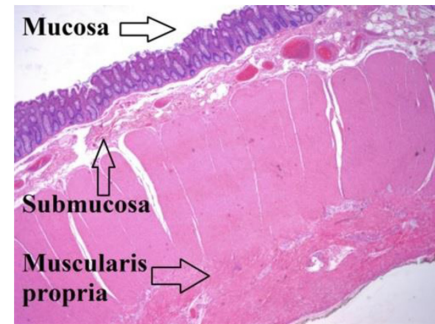
When spectral data are available for  $\mu'_s$  [ $\mu'_s(\lambda)$ ] [from inverse adding doubling (IAD) method applied to integrating sphere measurements of tissue sample optical properties], for the RI of scatterers [ $n_s(\lambda)$ ] and for the RI of ISF [ $n_0(\lambda)$ ], it is possible to try some  $a$  values in Eq. (2) to match data for  $\mu'_s$ .<sup>9</sup> Once the correct  $a$  value that allows such matching is obtained, the same equation can be used to calculate the time dependence for  $\mu'_s$ , provided that independent determination of the time dependencies for  $\bar{n}_0$  and  $f_s$  was made. If  $f_s(t=0)$ ,  $f_0(t=0)$  and the sample volume of natural tissue are known,  $f_s(t)$ ,  $f_0(t)$  can be calculated from  $d(t)$ .  $\bar{n}_0(t)$ , on the other hand, can be calculated with Eqs. (3) and (4). Once  $\mu'_s(t)$  is calculated with Eq. (2) and  $\mu_s(t)$  is calculated with Eq. (4), they can be used in Eq. (6) to obtain  $g(t)$ :<sup>9</sup>

$$g(t) = 1 - \frac{\mu'_s(t)}{\mu_s(t)}. \quad (6)$$

By estimating the time dependencies for the optical properties of biological tissues, treatment efficiency evaluation as a function of time or even pathology discrimination may be possible.

## 2.2 Tissue Samples

Due to the high incidence in human populations worldwide, colorectal cancer is a major health concern.<sup>35</sup> At an early stage of development, adenomatous polyps are formed in the inner layer of the colorectal wall, the mucosa—see Fig. 1.



(a)



(b)

**Fig. 1** (a) Histological cross section of human colorectal wall showing distinct layers and (b) the gross features of invasive colorectal adenocarcinoma (left) and adjacent mucosa viewed in a surgical specimen.

If not removed at an early stage, these polyps will evolve into adenocarcinoma that intrudes the other colorectal wall layers, first the submucosa, followed by the muscularis propria, and eventually reaching the peritoneal lining or adjacent organs.<sup>36</sup> Early stage detection and removal of colorectal polyps is very important and since they start developing in the mucosa, noninvasive endoscopic optical techniques are highly desired. Due to the distinct tissue layers in the colorectal wall, which have different optical properties, OC treatments might be a strong option to improve the development of such techniques for early or later stage polyp removal.

All normal and pathological tissue samples used in the present study were obtained from adult patients undergoing colorectal surgery at Portuguese Oncology Institute of Porto, Portugal. A signed consent allowing for the subsequent use of surgical specimens for diagnostic and research purposes was obtained previously to surgical procedures from all patients. This procedure has been approved by the Ethics Committee of Portuguese Oncology Institute of Porto.

After collecting the samples from surgical resection specimens, normal and pathological colorectal mucosa samples were separated and preserved frozen at  $-80^\circ\text{C}$  for a period of 12 h. A cryostat from Thermo Scientific™ (Waltham, Massachusetts), model Micron HM 550 was used to prepare samples to use in study with a circular form ( $\varphi = 1$  cm) and 0.5-mm thickness. To mimic natural hydration in tissue samples, they were kept in saline for 10 min before initiating studies. Both types of tissues were prepared and processed according to this standard protocol, meaning that any discrepancy related to the freezing procedure should be minimal.

A total of 16 normal and 16 pathological samples were used in measurements described in Secs. 2.3 and 2.4.

### 2.3 Total Water Content Evaluation

To obtain the total water content in normal and pathological tissues, we have performed a dehydration study, where 10 samples of each type were used. At the beginning of this study, all samples were weighted, before being placed inside a Memmert drying oven, model ULM 500 (Schwabach, Germany) for 24 h at a temperature of  $103^{\circ}\text{C} \pm 2^{\circ}\text{C}$ . The weight scale used was a Kern, model ALJ 220-4NM (Balingen, Germany) with a precision of  $\pm 0.0001\text{g}$ . After total dehydration, the samples were placed inside a desiccator for 15 min to remove any residual humidity at room temperature. Finally, the samples were weighted again. The average temperature for weight measurements before and after dehydration was  $22^{\circ}\text{C} \pm 2^{\circ}\text{C}$ .

As the initial volume of the samples was known before dehydration ( $V = \pi \times 0.5^2 \times 0.05\text{ cm}^3$ ), and considering that water has a density of  $1\text{ g/cm}^3$  at room temperature, the weight difference for each sample allowed us to calculate total water content. After averaging data from 10 normal and from 10 pathological tissue samples, we obtained a total water content of  $73.96\% \pm 0.02\%$  for normal mucosa and  $73.33\% \pm 0.10\%$  for pathological mucosa.

### 2.4 Thickness and $T_c$ Measurements

From our previous studies,<sup>19</sup> we have estimated the mobile water content in normal and pathological colorectal mucosa as 59.4% and 64.4%, respectively. Comparing between the total and mobile water contents of normal and pathological mucosa tissues, we see a decrease of 0.63% in total water and an increase of 5% in mobile water from normal to pathological. According to the literature,<sup>37</sup> bound water can be converted into mobile water when cancer cells invade the tissue. The significant increase in mobile water and some total water loss from normal to pathological mucosa was already seen for other tissues, as demonstrated by Fig. 7 of Ref. 38. The 5% difference in mobile water of mucosa tissues means that a glucose–water solution that will produce a smooth  $T_c$  time dependence during a 30 min OC treatment needs to have a glucose concentration of ~35% (for pathological mucosa) and ~40% (for normal mucosa). Thickness and  $T_c$  measurements were previously performed for these particular treatments at a mean temperature of  $20^{\circ}\text{C} \pm 0.5^{\circ}\text{C}$ ,<sup>19</sup> and the mean time dependencies resulting from those measurements were used in calculations performed in the present study. For thickness measurements, we used three normal and three pathological samples and for the  $T_c$  measurements the same number of samples was used to average final results. Figure 2(a) shows the setup used to measure sample thickness and Fig. 2(b) presents the  $T_c$  setup.

Considering the thickness measurements, the sample is placed inside two microscope glasses (thickness  $d_G = 1\text{ mm}$ ) and a digital micrometer from Mitutoyo<sup>TM</sup> (Japan), model 293 MDC-MX lite with a precision of 0.001 mm, measures the global thickness ( $D$ ).<sup>19</sup> The OC solution is injected in-between the glasses to begin treatment, and measurements are taken at every 15 s within the first 2 min and at every min after that. As the solution presents some viscosity, it stays within the glasses during all treatment, leading to a constant glucose flow into the tissue. At the end, the time dependence for sample thickness is obtained as the difference between the measurements and the fixed thickness of the glasses:  $d(t) = D(t) - (2 \times d_G)$ . Three studies were made for the treatment of pathological tissues with 35% of glucose and the other

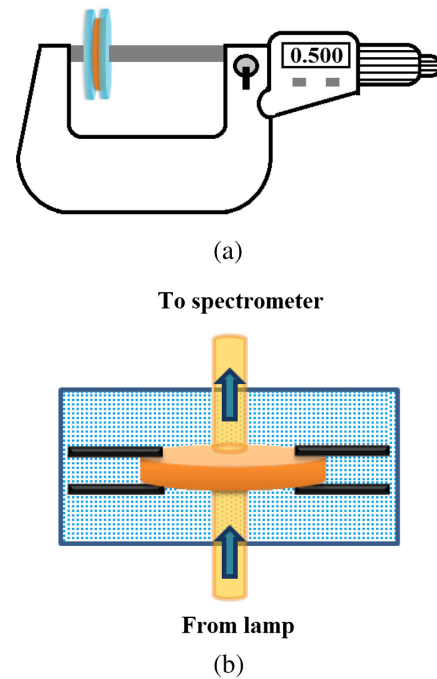


Fig. 2 Measurement setups for (a) thickness and (b)  $T_c$ .

three for the treatment of normal tissues with 40% of glucose. Mean thickness time dependence was calculated for each case. These results are presented in Ref. 19.

Considering  $T_c$  measurements, an Avalight-D(H)-S lamp from Avantes<sup>TM</sup> (The Netherlands) was used to irradiate the sample through an optical fiber cable and collimating lens. Light enters the sample cuvette [rectangular-box in Fig. 2(b)] through a glass at the bottom. The sample is fixed at the center of the cuvette by some wires, which are shown in Fig. 2(b) as black bars. A set of pinholes [not represented in Fig. 2(b)] guarantees a beam diameter of 1 mm between the illuminating and collecting optics. At the top of the cuvette, a second optical fiber cable and collimating lens collect the transmitted beam for delivery to the spectrometer. The  $T_c$  spectrum of the natural sample is measured first. Then, the OC solution [represented as small dots in the cuvette of Fig. 2(b)] is injected into the cuvette by a syringe through a lateral hole. Spectra are measured during treatment at every 5 s for a period of 30 min. Three sets of  $T_c$  studies were made for the treatment of pathological mucosa with 35% of glucose and the other three were made for the treatment of normal mucosa with 40% of glucose. Mean time dependencies for  $T_c$  spectra were calculated in each case and can be found in Ref. 19.

### 2.5 Reconstruction of $\mu'_s$ for Natural Tissue

To obtain the time dependencies for the optical properties of normal and pathological colorectal mucosa with accuracy, a complete study with different types of measurements should be made during treatments. Such study is complex and it involves a large number of tissue samples (normal and pathological) to be studied under different measurement procedures. As explained above when we introduced Eq. (2), such an equation was validated only for specific conditions and for samples whose scatterers are spherical. This is definitely not the case for the tissues we used in this study as it has been reported that normal and pathological colorectal mucosa contains scatterers—like collagen fibrils

and myofibroblasts in stroma,<sup>39</sup> and different types of proteins,<sup>40</sup> such as glycoproteins.<sup>41</sup> As we wanted to test Eq. (2) outside the limits where it was validated, to confirm the theoretical predictions of scattering coefficients decrease and anisotropy increase and possibly differentiate between treatment response of normal and pathological tissues, we had to select an estimation method. In the absence of a more accurate model and to avoid a complex experimental study to estimate the time dependencies for the optical properties of human colorectal mucosa, we selected to perform the calculations based on Eq. (2).

The first calculation consisted of reconstructing the wavelength dependence for  $\mu'_s$  through Eq. (2) with the objective of estimating  $a$  for each tissue. In this calculation, we are able to determine also the correct  $\bar{n}_0(\lambda)$  and  $n_s(\lambda)$  for the natural tissues, which are necessary for further calculations. The following reconstruction procedure was used for both tissues.

Considering as reference the  $\mu'_s(\lambda)$  data that were previously estimated via IAD simulations<sup>42</sup> for natural tissues (presented in Ref. 43), we performed the following steps:

- I. Calculation of the dispersion for dry matter by subtracting the contribution of total water from the dispersion of the tissue that we have estimated in a previous study.<sup>44</sup> This calculation was made for both tissues according to Eqs. (7) and (8):

$$n_{\text{dry-n}}(\lambda) = \frac{n_{\text{tissue-n}}(\lambda) - 0.7396 \times n_{\text{H}_2\text{O}}(\lambda)}{1 - 0.7396}, \quad (7)$$

$$n_{\text{dry-p}}(\lambda) = \frac{n_{\text{tissue-p}}(\lambda) - 0.7333 \times n_{\text{H}_2\text{O}}(\lambda)}{1 - 0.7333} \quad (8)$$

where  $n_{\text{H}_2\text{O}}(\lambda)$  is the dispersion of water at 20°C (average temperature during our experimental measurements), as retrieved from literature,<sup>45</sup>  $n_{\text{tissue-n}}(\lambda)$  is the dispersion of normal mucosa,  $n_{\text{tissue-p}}(\lambda)$  is the dispersion of pathological mucosa,  $n_{\text{dry-n}}(\lambda)$  is the dispersion of scatterers in normal mucosa, and  $n_{\text{dry-p}}(\lambda)$  is the dispersion of scatterers in pathological mucosa.

- II. Calculation of scatterers dispersion,  $n_s(\lambda)$ , in the tissue by combining the dispersions of dry matter and water through Gladstone and Dale law [Eq. (5)].
- III. Again, using Gladstone and Dale law, we calculated ISF dispersion,  $\bar{n}_0(\lambda)$ , by subtracting the scatterer contribution from tissue dispersion with appropriate VFs.
- IV. Calculation of the wavelength dependence for the relative index,  $m(\lambda)$ , through Eq. (1).
- V. Using  $\bar{n}_0(\lambda)$ ,  $m(\lambda)$ , and  $f_s$  that were estimated in previous steps, we reconstructed  $\mu'_s(\lambda)$  with a particular value of  $a$ , in a new form of Eq. (2):<sup>9</sup>

$$\mu'_s(\lambda) = \frac{3f_s(1-f_s)}{4\pi a^3} \times 3.28\pi a^2 \left[ \frac{2\pi\bar{n}_0(\lambda)a}{\lambda} \right]^{0.37} [m(\lambda) - 1]^{2.09}. \quad (9)$$

The above-described procedure was made by trial and error until the reconstruction of  $\mu'_s(\lambda)$  was obtained correctly. In the first trials, the calculated  $\mu'_s(\lambda)$  was too far from the values estimated through IAD simulations. To correct this, we had to adjust the VFs in the calculation of the dispersions for scatterers and ISF (steps II and III above). These adjustments also produce a change in  $m(\lambda)$ . When the calculated  $\mu'_s(\lambda)$  was approaching the IAD estimated data, we changed  $a$  for a better matching.

The estimated  $\mu'_s(\lambda)$ ,  $\bar{n}_0(\lambda)$ ,  $n_s(\lambda)$ , corresponding VFs for scatterers and ISF in natural tissue and the  $a$  value were considered in further calculations described in the following subsections.

## 2.6 Calculation of Kinetics for $\mu_s$ , $\bar{n}_0$ , and $n_{\text{tissue}}$

To calculate the kinetics for  $\mu_s$ , we needed the wavelength dependence for  $\mu_a$ , which is presented in Ref. 43 for both tissues. Considering this data and the  $T_c$  measurements made from natural tissues and during treatments, we used Eq. (4) to obtain  $\mu_s(\lambda, t)$ .

Once these data were calculated, we have used Eq. (3) to calculate  $\bar{n}_0(\lambda, t)$ . In this calculation, the mean  $d(t)$  measurements obtained for each tissue/treatment were also used.

To calculate the time dependence for the RI of the whole tissue [ $n_{\text{tissue}}(\lambda, t)$ ] with Eq. (5), we needed  $f_s(t)$  and  $f_0(t)$  in each tissue. Considering the thickness measurements made from normal and pathological tissues during corresponding treatments, these time dependencies were obtained as follows:

- I. Considering form and dimensions of natural samples, their total volume was calculated as

$$V_{\text{tissue}}(t=0) = (\pi \times 0.5^2) \times 0.05 \text{ cm}^3 \quad (10)$$

- II. The absolute volume for scatterers in the tissue was calculated considering their appropriate VFs in each tissue:

$$V_{\text{scat}} = V_{\text{tissue}}(t=0) \times f_s(t=0) \text{ cm}^3 \quad (11)$$

where  $f_s(t=0) = 0.4$  for normal mucosa, and  $f_s(t=0) = 0.35$  for pathological mucosa.<sup>19</sup>

- III. This volume remains unchanged during treatment, whereas  $f_s$  changes according to

$$f_s(t) = \frac{V_{\text{scat}}}{(\pi \times 0.5^2) \times d(t)} \quad (12)$$

where  $d(t)$  is the time dependence of sample thickness for normal or pathological mucosa.

- IV. As, according to Gladstone and Dale law,  $f_0(t) + f_s(t) = 1$ , we could calculate  $n_{\text{tissue}}(\lambda, t)$  with Eq. (5).

## 2.7 Calculation of Kinetics for $\mu'_s$ and $g$

To calculate the kinetics for  $\mu'_s$ , we used Eq. (9), but now considering the time dependence for the VF of scatterers,  $f_s(t)$ , instead of its value for natural tissue. Furthermore, instead of using  $\bar{n}_0(\lambda)$  and  $m(\lambda)$  for the natural tissues, we used their

time dependencies,  $\bar{n}_0(\lambda, t)$  and  $m(\lambda, t)$ , as calculated with the procedure described in Sec. 2.6.

Once the kinetics of  $\mu'_s$  was obtained, we used Eq. (6) to calculate the kinetics for  $g(\lambda)$ .

All the results of these calculations for normal and pathological tissues are presented in Sec. 3.

### 3 Results and Discussion

#### 3.1 Data Estimation for Natural Tissue

To calculate the kinetics for the optical properties of tissues under study, we needed to start by estimating the spectral data for the RI of scatterers and ISF and the mean scatterer radius. To obtain these data, we have initiated our calculations by reconstructing  $\mu'_s(\lambda)$ , as indicated in Sec. 2.5. Such reconstruction was made by adjusting  $n_s(\lambda)$ ,  $\bar{n}_0(\lambda)$ , and  $a$ . The dispersions that provided the best reconstruction of  $\mu'_s(\lambda)$  for both tissues are shown in Fig. 3.

The dispersions obtained for normal mucosa that is shown in Fig. 3(a) are described by the following equations [whole tissue—Eq. (13), ISF—Eq. (14), and scatterers—Eq. (15)]:

$$n_{n\text{-tissue}}(\lambda) = 1.315 + \frac{16.73}{\lambda - 38.84}, \tag{13}$$

$$n_0(\lambda) = 1.309 + \frac{16.58}{\lambda - 9.636}, \tag{14}$$

$$n_s(\lambda) = 1.325 + \frac{17.32}{\lambda - 68.94}. \tag{15}$$

For the case of pathological mucosa, the following equations describe the curves presented in Fig. 3(b) [whole tissue—Eq. (16), ISF—Eq. (17), and scatterers—Eq. (18)]:

$$n_{n\text{-tissue}}(\lambda) = 1.315 + \frac{19.25}{\lambda - 46.83}, \tag{16}$$

$$n_0(\lambda) = 1.307 + \frac{19.52}{\lambda + 4.278}, \tag{17}$$

$$n_s(\lambda) = 1.329 + \frac{20.22}{\lambda - 98.00}. \tag{18}$$

Using the dispersions for scatterers and ISF presented in Fig. 3 for both tissues, we calculated the relative indices of natural tissues, which are shown in Fig. 4.

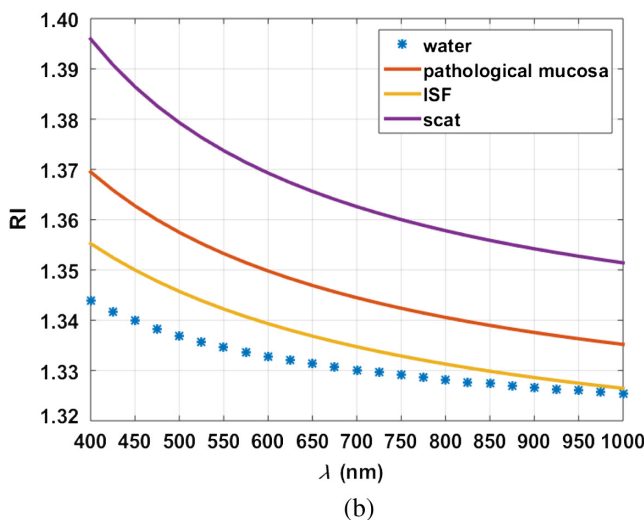
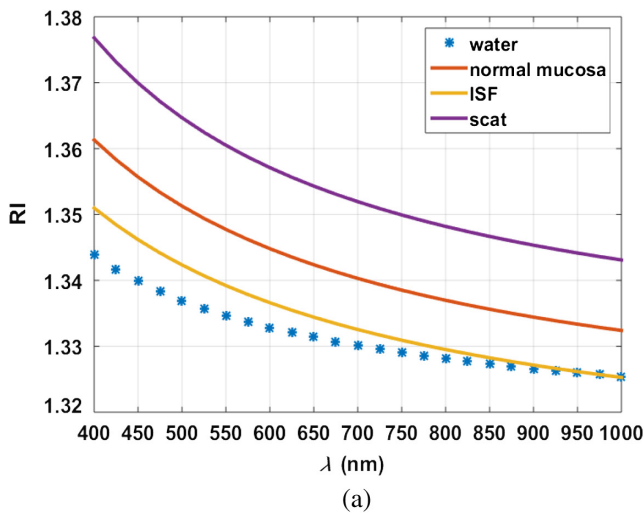


**Fig. 3** Dispersions for water,<sup>45</sup> colorectal mucosa, its scatterers and ISF at 20°C. (a) Normal mucosa and (b) pathological mucosa.

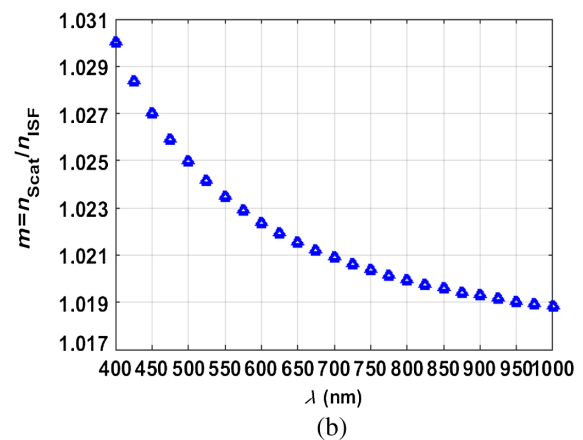
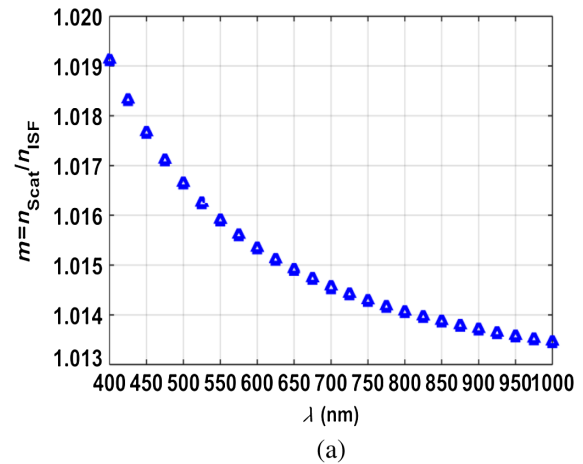


**Fig. 4** Relative index for natural tissue. (a) Normal mucosa and (b) pathological mucosa.

Using all the calculated dispersions for scatterers and ISF and the VF of scatterers in Eq. (9), we obtained a good reconstruction for  $\mu'_s(\lambda)$  data of both tissues, by considering the correspondent scatterer radius,  $a$ , as: 46-nm (normal mucosa) and 158-nm (pathological mucosa).

Considering that collagen fibrils are the main scatterers in colorectal mucosa stroma underlying the epithelium,<sup>46</sup> we performed a simple calculation to check the accuracy of these results. Collagen fibrils have a cylinder-shape, and making length and diameter measurements from electronic micrographs of normal mucosa tissue in Ref. 47, we estimated the mean fibril length as 0.119  $\mu\text{m}$  and the mean radius as 0.039  $\mu\text{m}$ . Considering these values, the mean volume can be calculated:

$$V_{\text{fibril}} = (\pi r^2) \times h = 5.69 \times 10^{-4} \mu\text{m}^3. \tag{19}$$

Using this volume, we can calculate the mean radius for an equivalent sphere model as

$$R_{\text{sphere}} = \sqrt[3]{\frac{5.69 \times 10^{-4}}{\pi} \times \frac{3}{4}} = 0.0514 \mu\text{m} = 51.4 \text{ nm} \tag{20}$$

Comparing this value with the mean estimated radius for normal mucosa (46 nm), we see that calculations using Eq. (2)

are not precise, but they show that the spherical scatterer model is not too bad to approximate real fibril scatterers in tissues. The values measured from Ref. 47 refer to collagen fibrils in oral mucosa, but smaller collagen diameters can be found in other tissues like in Fig. 3 of Ref. 48 for the eye sclera.

Regarding pathological tissues, we could not compare our estimated sizing data with real data from the literature, but as indicated by some authors,<sup>49-51</sup> when cancer invades mucosal stroma, collagen fibrils increase in the length, diameter, and density. This means that the estimations we made with Eq. (2) are sensitive to the mean scatterer size increase from normal to pathological tissue.

Previously estimated  $\mu_a(\lambda)$  and  $\mu'_s(\lambda)$  data and reconstructed  $\mu'_s(\lambda)$  curves with Eq. (9) are shown in Fig. 5.

From Fig. 5, we see similar wavelength dependencies for normal and pathological tissues but with pathological tissues showing more blood content. From graphs in Figs. 5(c) and 5(d), we see that the calculated curves provide good fittings of the data previously estimated with IAD simulations. For the case of pathological mucosa, some estimated points between 500 and 600 nm are not in agreement with the calculated curve, meaning that some cross talk between absorption and scattering near hemoglobin bands changes the smooth decreasing behavior as calculated with Eq. (9). We do not see significant evidence of such behavior in normal mucosa, indicating that pathological tissues have higher blood content, which is accordingly to

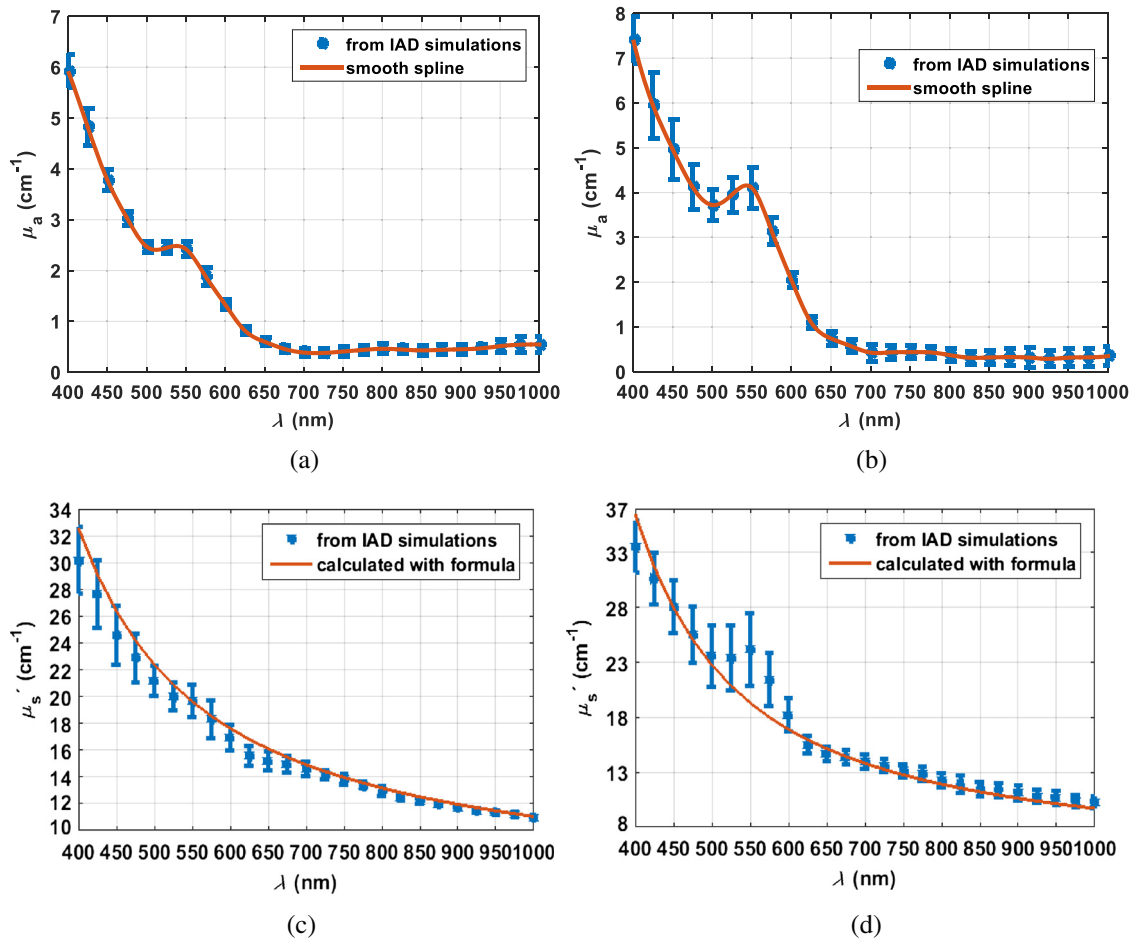


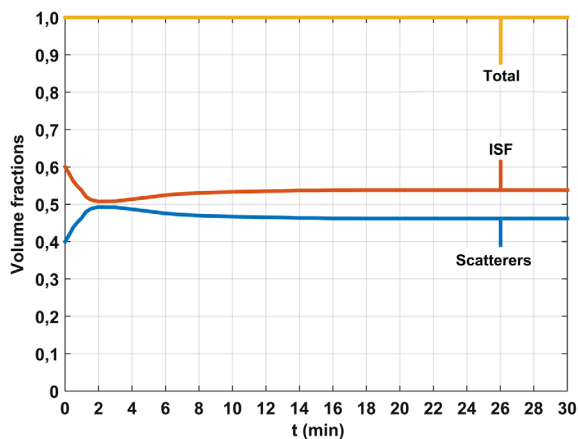
**Fig. 5** Estimated  $\mu_a(\lambda)$  data for (a) normal mucosa and (b) pathological mucosa. Estimated and calculated  $\mu'_s(\lambda)$  data for (c) normal mucosa and (d) pathological mucosa.

the reddish color seen in Fig. 1(b) for the adenocarcinoma. A different equation that accounts for the Rayleigh and Mie scattering terms can be used to describe the curves shown in graphs of Figs. 5(c) and 5(d), respectively. Such equation is described by Steven Jacques in his paper from 2013,<sup>52</sup> and if we fit the calculated data (curves) in graphs of Figs. 5(c) and 5(d) with that equation, we obtain optimized fitting ( $R^2 = 1$ ) for both types of tissues:

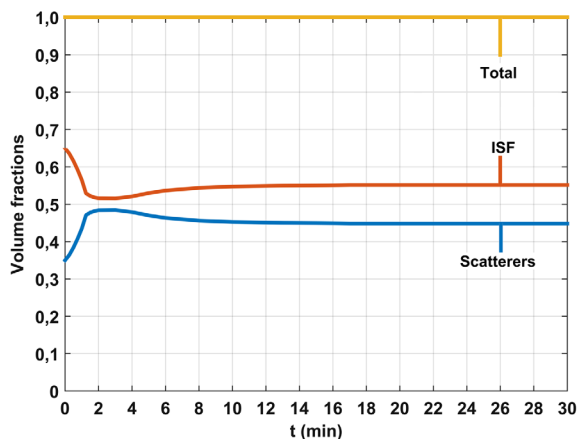
$$\mu'_{s\text{-normal}}(\lambda) = 22.32 \times \left[ 0.2318 \times \left( \frac{\lambda}{500} \right)^{-4} + (1 - 0.2318) \times \left( \frac{\lambda}{500} \right)^{-0.6874} \right], \quad (21)$$

$$\mu'_{s\text{-pathol}}(\lambda) = 22.73 \times \left[ 0.3423 \times \left( \frac{\lambda}{500} \right)^{-4} + (1 - 0.3423) \times \left( \frac{\lambda}{500} \right)^{-0.703} \right]. \quad (22)$$

Now that we have estimated the mean scatterer radius for normal and pathological tissues, we need to calculate the kinetics of the RI of ISF to proceed with calculation for the kinetics of  $\mu'_s$ . The following subsection presents the results for the kinetics of RI.



(a)



(b)

**Fig. 6** Time dependence for the VFs of colorectal mucosa during treatment. (a) Normal mucosa treated with 40% of glucose and (b) pathological mucosa treated with 35% of glucose.

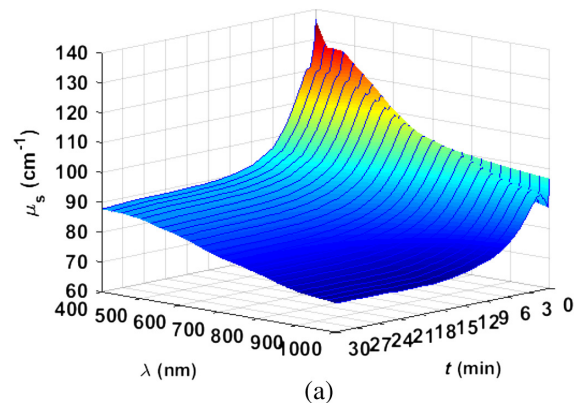
### 3.2 Kinetics for $\mu_s(\lambda)$ , $\bar{n}_0$ , and $n_{\text{tissue}}$

Using the procedure outlined in Sec. 2.6, we started by calculating the time dependence for the VFs of ISF and scatterers. Figure 6 presents these variations for both tissues.

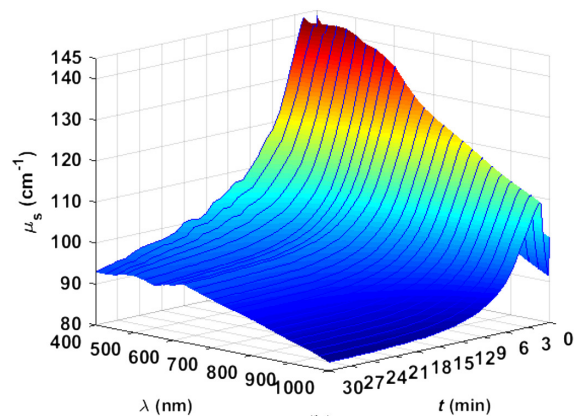
Graphs in Fig. 6 show a fast and strong variation in VFs for both tissues within the first two minutes, indicating the occurrence of the dehydration mechanism, which dominates at early stage treatment. After 3 min, VFs show smooth and low-magnitude variations, meaning that they are now driven by the RI matching mechanism that occurs in the interstitial locations. Figure 6 shows evidence of the two OC mechanisms and give an idea of their duration. Similar behavior is observed for both mucosa tissues, but the magnitude of the variations that correspond to the dehydration mechanism is higher for pathological mucosa.

Using  $\mu_a(\lambda, t = 0)$ ,  $T_c(\lambda, t)$ , and  $d(t)$  data in Eq. (4), we calculated the time dependencies for  $\mu_s(\lambda)$  in both tissues. Those graphs are shown in Fig. 7.

In this case, we see that both tissues present a decreasing behavior over the time of treatment as expected for OC treatments. There is some transient decreasing behavior within the first seconds of treatment for long wavelengths in both tissues, possibly due to interaction of OCA with superficial layers of tissues. After that and within the first 2 min, both tissues show an increase in  $\mu_s$ , which indicates the approximation of scatterers due to the loss of water in the interstitial locations. Such increase seems to have higher magnitude near the absorption bands of hemoglobin and in particular for pathological mucosa.



(a)



(b)

**Fig. 7** Kinetics of  $\mu_s$  for (a) normal mucosa and (b) pathological mucosa.

The water and blood contents in natural tissues originate these differences between normal and pathological tissues for the kinetics of  $\mu_s$ : natural pathological mucosa has less water content than normal mucosa (see Fig. 3) and higher blood content than normal mucosa (see Fig. 5).

Regarding the subsequent smooth decrease, both types of tissues present similar behavior, where the longer wavelengths show high magnitude decrease. For smaller wavelengths, the decrease in  $\mu_s$  is modest due to the presence of the absorption bands of blood. The data shown in graphs of Fig. 7 indicate that the simple model we used confirms the expectation of a global decreasing in  $\mu_s$  during OC treatments. It shows also that normal and pathological tissues have similar variations in  $\mu_s$  during treatment.

Using the obtained  $\mu_s$  data in Eq. (3), we calculated the kinetics of  $\bar{n}_0$  for both tissues and combining that data with the dispersion of scatterers in Eq. (5), we calculated the kinetics for tissue RI for both tissues. Figure 8 shows these graphs.

As expected, the RI of ISF increases with treatment, showing the evidence of the RI matching mechanism. For the case of normal mucosa, we see a smooth behavior for all wavelengths and during all treatment. For pathological mucosa, the overall effect and magnitude of the increase are similar to normal mucosa, but a significant change of form in dispersion is seen for lower wavelengths at the beginning of treatment.

The graphs for  $n_{\text{tissue}}$  in Figs. 8(c) and 8(d) present three stages: within the first min, a strong increase in  $n_{\text{tissue}}$  corresponds to the dehydration mechanism; a transition between mechanisms is seen in the following 3 min; and the RI matching

mechanism dominates over the following 26 min. Although the overall behavior is similar between tissues, for the case of pathological mucosa we see a higher magnitude increase at the beginning, which is conditioned by the water content in natural pathological mucosa. As the water content in untreated pathological mucosa is smaller than in untreated normal mucosa (see Fig. 3), it takes less time for the dehydration mechanism to occur in pathological tissues.

### 3.3 Kinetics for $\mu'_s(\lambda)$ and $g$

According to the procedure described in Sec. 2.7, we first calculated the time dependencies for the relative index of refraction for both tissues. Then using these data and Eq. (9), we calculated the time dependencies for  $\mu'_s(\lambda)$ . Combining these data with the data in Fig. 7 by using Eq. (6), we calculated the time dependencies for  $g$ -factor for both tissues. Figure 9 shows all these graphs for both tissues.

Considering graphs (a) and (b) of Fig. 9, we see that the relative index of refraction shows similar decreasing behavior for both tissues and a higher magnitude decrease is observed for pathological mucosa. The kinetics of  $\mu'_s(\lambda)$  presented in graphs (c) and (d) of Fig. 9 show a smoother behavior than the one observed for  $\mu_s(\lambda)$  (see Fig. 7), more similar to the kinetics of  $m$ , and no significant differences are seen between normal and pathological mucosa in this case. To show this decreasing behavior over the time of treatment, we had to select the presented perspective in graphs (c) and (d) of Fig. 9, which does not show a slight increase in  $\mu'_s(\lambda)$  from  $t = 0$  to  $t = 15$  s.

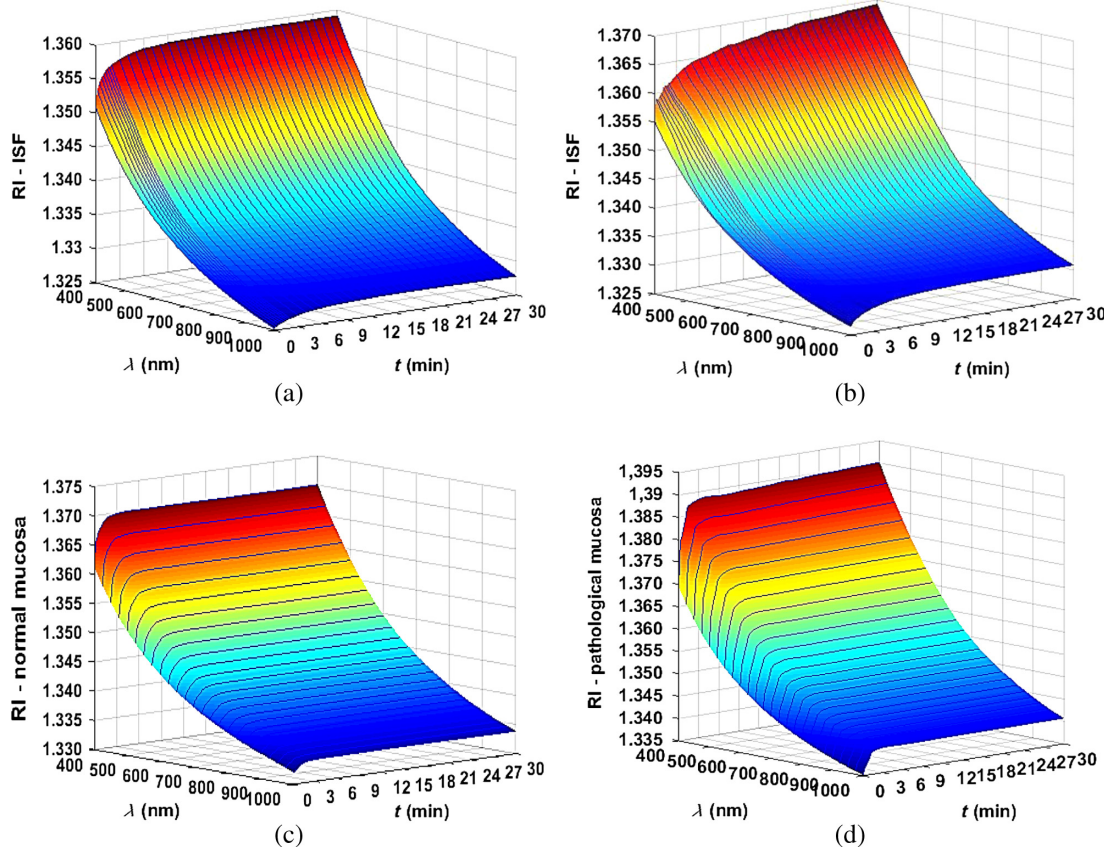


**Fig. 8** Kinetics of  $\bar{n}_0$  for (a) normal mucosa and (b) pathological mucosa, and kinetics of  $n_{\text{tissue}}$  for (c) normal mucosa and (d) pathological mucosa.

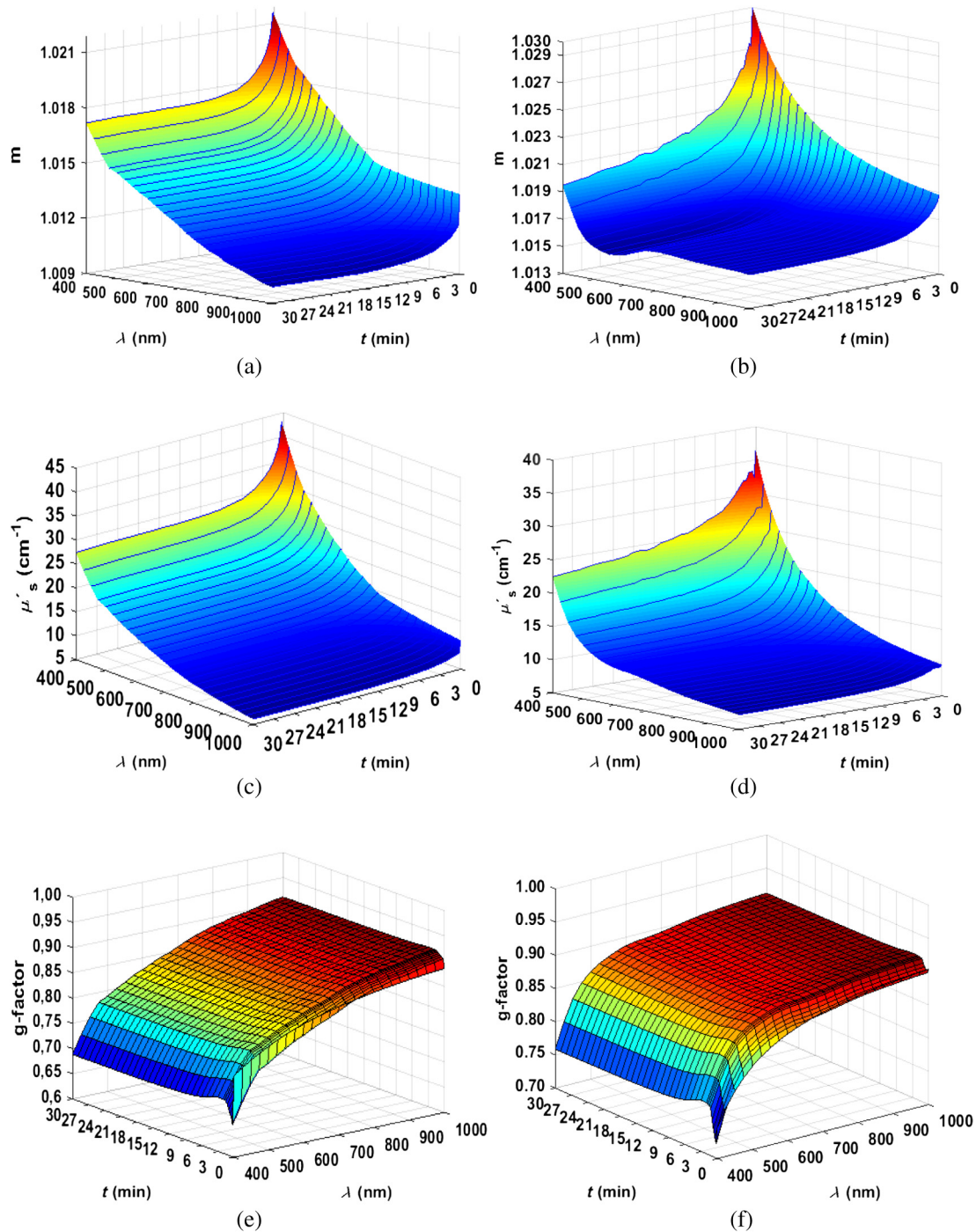


**Fig. 9** Kinetics of  $m$  for (a) normal mucosa and (b) pathological mucosa; kinetics of  $\mu'_s$  for (c) normal mucosa and (d) pathological mucosa; kinetics of  $g$  for (e) normal mucosa and (f) pathological mucosa.

Graphs (e) and (f) of Fig. 9 plot a change in the form of  $g(\lambda)$  at the beginning of treatment for both tissues, where longer wavelengths show a significant decrease for normal mucosa. We have seen similar transient behavior for  $\mu_s$  in Fig. 7, and it is possibly related to the early interaction of glucose molecules with superficial tissue layers. Immediately after, we see a strong and fast increase. As water loss leads to a better packing inside the tissue, forward scattering increases.

Due to the transition between dehydration and RI matching mechanisms, we see a small decrease in  $g$  after 2 min for both tissues. Such decrease is originated by the separation of

scatterers as glucose molecules place themselves in the interstitial locations.<sup>9</sup>

Using confocal microscopy, a group from the Department of Dermatology of the Oregon Health and Science University has reported in 2010 the increase in  $g$  during optical clearing of skin,<sup>53</sup> which accords with our calculations. In that same study, no significant changes in  $\mu_s$  were observed. This study regards the treatment of skin samples with 80% of DMSO, and pure glycerin solutions and measurements were made only before and after 1 h treatment. Considering their results and the ones from the present study, we must consider that

skin is a multilayered tissue with a set of optical properties per layer, whereas colorectal mucosa has only a set of optical properties. Another major difference that might lead to insignificant change in  $\mu_s$  in their study is that they used oversaturated solutions. As we have demonstrated in a previous study,<sup>24</sup> when the water in the treating solution matches the mobile water in the tissue (intermediate OCA concentrations in solution), only the RI matching mechanism occurs, as minimal or no water flux is observed. This is approximately the case for the treatments presented here—normal mucosa treated with 40% of glucose and pathological mucosa treated with 35% of glucose.<sup>19</sup> Under these conditions, the unique OCA flux into the interstitial locations of the tissue is smooth and continuous. Such process leads to a reduction of  $\mu_s$ , through the RI matching mechanism and an increase in the  $g$ -factor as our calculations demonstrate. When oversaturated solutions are used, as in the case of the study presented in Ref. 53, the dehydration mechanism will dominate OC during early stage treatment, as we have also previously demonstrated.<sup>24</sup> During this early stage dehydration, the water loss by the tissue forces scatterers to approach each other and to form better packing (scatterers change their random orientations into the same direction). Such scatterer alignment leads to an increase in the  $g$ -factor. When treating normal and pathological colorectal mucosa samples with 54% of glucose,<sup>19</sup> we observed an initial  $T_c$  increase, followed by a decrease. These  $T_c$  variations indicate that the glucose molecules initially diffuse into the interstitial space of the tissues and then into the tissue cells. OCA diffusion into tissue cells increases  $\mu_s$  due to scatterer size increase. For a long treatment with oversaturated solutions, as in the case of Ref. 53, it is expected that the overall variations are some increase in  $g$ -factor (due to better alignment of scatterers) and minimal change in  $\mu_s$  (due to mutual compensation of RI matching effect and increased scattering efficiency caused by scatterer density elevation).

## 4 Conclusions

The kinetics of the optical properties of human normal and pathological colorectal mucosa were evaluated with a simple and indirect method based on thickness and  $T_c$  measurements during treatments with glucose–water solutions (35% for pathological and 40% for normal mucosa). The first calculations made with this model have estimated that the mean scatterer radius in normal mucosa is 46 nm and in pathological mucosa is 158 nm. Although this method is not precise, we demonstrated that the estimated mean scatterer size is not bad and that Eq. (2) is sensitive to scatterer size increase from normal to pathological tissues, as expected. We also verified that this equation can be used outside the limits where it was initially validated. The results presented in this study show the expected kinetics for the optical properties of tissues during OC treatments and indicate that the method is sensitive to the two OC mechanisms—tissue dehydration and RI matching. No significant differences were observed between the kinetics of the optical properties for normal and pathological tissues, meaning that both tissues respond in the same manner to the treatments—decrease in the scattering coefficients and increase in  $g$ -factor. The evaluation of those kinetics for wavelengths between 400 and 1000 nm allowed to see that the water and blood contents in untreated normal and pathological tissues conditions time dependencies result from the applied treatments. Such spectral data are also valuable for kinetics comparison between different wavelengths. Some initial OCA

impact on the tissue was detected for both tissues in the kinetics of  $\mu_s$  and  $g$ , where a fast decrease in these properties was followed by an increase in the first seconds of treatment. The increase in  $\mu_s$  and  $g$ -factor indicates the better packing of tissue scatterers that is momentarily created by tissue dehydration. After these initial variations, we see that glucose diffusion into the tissues produces a reduction in the scattering coefficients through the RI matching mechanism.

By obtaining the time dependencies for the optical properties of both tissues, we acquired valuable information. For instance, a specific treatment duration can be selected to obtain a particular set of optical properties that correspond to a desired tissue transparency. Such information can be very useful in future planning of diagnosis or treatment procedures of colorectal cancer where OC treatments are used. The calculation procedure used in this research can be applied to other tissues/treatments to estimate the time dependence of the optical properties and characterize those treatments. Before those calculations can be made for real biological tissues, the model based on Eq. (2) must be corrected and we plan to work on a more realistic version of that equation.

## Disclosures

The authors have no relevant financial interests in this article and no potential conflicts of interest to disclose.

## Acknowledgments

This research has been supported by the Portuguese Foundation for Science and Technology: Award no. UID-EQU-04730-2013 and by the Russian Foundation for Basic Research: Award no. 18-29-02060.

## References

1. V. V. Tuchin, *Optical Clearing of Tissues and Blood*, SPIE Press, Bellingham, Washington (2006).
2. H. Liu et al., "Dependence of tissue optical properties on solute-induced changes in refractive index and osmolarity," *J. Biomed. Opt.* **1**(2), 200–211 (1996).
3. R. Graaff et al., "Reduced light-scattering properties for mixtures of spherical particles: a simple approximation derived from Mie calculations," *Appl. Opt.* **31**(10) 1370–1376 (1992).
4. V. V. Tuchin et al., "Light propagation in tissues with controlled optical properties," *J. Biomed. Opt.* **2**(4), 401–407 (1997).
5. E. A. Genina et al., "Optical clearing of biological tissues: prospects of application in medical diagnostics and phototherapy," *J. Biomed. Photonics Eng.* **1**(1), 22–58 (2015).
6. A. Y. Sdobnov et al., "Recent progress in tissue clearing for spectroscopic application," *Spectrochim. Acta Part A* **197**, 216–229 (2018).
7. D. S. Richardson and J. W. Lichtman, "Clarifying tissue clearing," *Cell* **162**(2), 246–257 (2015).
8. L. Oliveira et al., "Optical clearing mechanisms characterization in muscle," *J. Innovative Opt. Health Sci.* **9**(5), 1650035 (2016).
9. I. Carneiro et al., "Kinetics of optical properties of colorectal muscle during optical clearing," *J. Sel. Top. Quantum Electron.* **25**(1), 7200608 (2019).
10. D. Zhu et al., "Recent progress in tissue optical clearing," *Laser Photonics Rev.* **7**(5), 732–757 (2013).
11. E. A. Genina et al., "Tissue optical immersion clearing," *Expert Rev. Med. Devices* **7**(6), 825–842 (2010).
12. C. Choe et al., "Depth profiles of hydrogen bound water molecule types and their relation to lipid and protein interaction in the human stratum corneum in vivo," *Analyst* **141**(22), 6329–6337 (2016).
13. V. Gillard et al., "Measurement of total water and bound water content in human stratum corneum by in vitro proton nuclear magnetic resonance spectroscopy," *Int. J. Cosmet. Sci.* **20**(2), 117–125 (1998).

14. H. Hama et al., "Scale: a chemical approach for fluorescence imaging and reconstruction of transparent mouse brain," *Nat. Neurosci.* **14**(11), 1481–1488 (2011).
15. P. Matryba et al., "Optimized perfusion-based CUBIC protocol for the efficient whole-body clearing and imaging of rat organs," *J. Biophotonics* **11**(5), e201700248 (2018).
16. Sdobnov et al., "Hydrogen bound water profiles in the skin influenced by optical clearing molecular agents—quantitative analysis using confocal Raman microscopy," *J. Biophotonics* (accepted).
17. C. Choe et al., "Human skin in vivo has a higher skin barrier function than porcine skin ex vivo—comprehensive Raman microscopic study of the stratum corneum," *J. Biophotonics* **11**(6), e201700355 (2018).
18. A. Sdobnov et al., "Confocal Raman microscopy supported by optical clearing treatment of the skin—influence on collagen hydration," *J. Phys. D Appl. Phys.* **50**(28), 285401 (2017).
19. S. Carvalho et al., "Glucose diffusion in colorectal mucosa—a comparative study between normal and cancer tissues," *J. Biomed. Opt.* **22**(9), 091506 (2017).
20. B. Schultz et al., "Spectroscopic ellipsometry on biological materials—investigation of hydration dynamics and structural properties," *Thin Solid Films* **455**, 731–734 (2004).
21. A. A. Gurjarpathye et al., "Effect of localized mechanical indentation on skin water content evaluated using OCT," *Int. J. Biomed. Imaging* **2011**, 1–8 (2011).
22. C. X. Li et al., "The variations of water in human tissue under certain compression: studied with diffuse reflectance spectroscopy," *J. Innov. Opt. Health Sci.* **6**(1), 1350005 (2013).
23. L. Oliveira et al., "The characteristic time of glucose diffusion measured for muscle tissue at optical clearing," *Laser Phys.* **23**(7), 075606 (2013).
24. L. Oliveira et al., "Diffusion characteristics of ethylene glycol in skeletal muscle," *J. Biomed. Opt.* **20**(5), 051019 (2015).
25. D. K. Tuchina et al., "Study of glycerol diffusion in skin and myocardium ex vivo under the conditions of developing alloxan-induced diabetes," *J. Biomed. Photonics Eng.* **3**(2), 020302 (2017).
26. V. D. Genin et al., "Polyethylene Glycol diffusion in ex vivo skin tissue," *AIP Conf. Proc.* **1688**, 030028 (2015).
27. I. Carneiro et al., "Simple multimodal optical technique for evaluation of free/bound water and dispersion of human liver tissue," *J. Biomed. Opt.* **22**(12), 125002 (2017).
28. V. D. Genin et al., "Ex vivo investigation of glycerol diffusion in skin tissue," *J. Biomed. Photonics Eng.* **2**(1), 010303 (2016).
29. L. Oliveira et al., "Skeletal muscle dispersion (400–1000 nm) and kinetics at optical clearing," *J. Biophotonics* **11**(1), e201700094 (2018).
30. V. V. Tuchin, *Tissue Optics: Light Scattering Methods and Instruments for Medical Diagnosis*, 3rd ed., SPIE Press, Bellingham, Washington (2015).
31. D. W. Leonard and K. M. Meek, "Refractive indices of the collagen fibrils and extrafibrillar material of the corneal stroma," *Biophys. J.* **72**(3), 1382–1387 (1997).
32. K. M. Meek et al., "Changes in the refractive index of the stroma and its extrafibrillar matrix," *Biophys. J.* **85**(4), 2205–2212 (2003).
33. K. M. Meek et al., "Transparency, swelling and scarring in the corneal stroma," *Eye* **17**(8), 927–936 (2003).
34. O. Zhernovaya et al., "The refractive index of human hemoglobin in the visible range," *Phys. Med. Biol.* **56**(13), 4013–4021 (2011).
35. H. Brenner et al., "Colorectal cancer," *Lancet* **383**(9927), 1490–1502 (2014).
36. A. Pierangelo et al., "Ex-vivo characterization of human colon cancer by Mueller polarimetric imaging," *Opt. Express* **19**(2), 1582–1593 (2011).
37. P. A. Adegboyeda et al., "Immunohistochemical study of myofibroblasts in normal colonic mucosa, hyperplastic polyps, and adenomatous colorectal polyps," *Arch. Pathol. Lab Med.* **126**(7), 829–836 (2002).
38. I. C. Kiricuta, Jr. and V. Simplăceanu, "Tissue water content and nuclear magnetic resonance in normal and tumor tissues," *Cancer Res.* **35**, 1164–1167 (1975).
39. S. H. Chung et al., "In vivo water state measurements in breast cancer using broadband diffuse optical spectroscopy," *Phys. Med. Biol.* **53**(23), 6713–6727 (2008).
40. M. I. Koukourakis et al., "Comparison of metabolic pathways between cancer cells and stromal cells in colorectal carcinomas: a metabolic survival role for tumor-associated stroma," *Cancer Res.* **66**(2), 632–637 (2006).
41. M. I. Filipe, "Mucous secretion in rat colonic mucosa during carcinogenesis induced by dimethylhydrazine. A morphological and histochemical study," *Br. J. Cancer* **32**(1), 60–77 (1975).
42. S. A. Prah et al., "Determining the optical properties of turbid media by using the adding-doubling method," *Appl. Opt.* **32**(4), 559–568 (1993).
43. S. Carvalho et al., "Comparative study of the optical properties of colon mucosa and colon precancerous polyps between 400 and 1000 nm," *Proc. SPIE* **10063**, 100631L (2017).
44. I. Carneiro et al., "Water content and scatterers dispersion evaluation in colorectal tissues," *J. Biomed. Photonics Eng.* **3**(4), 040301 (2017).
45. M. Daimon and A. Masumura, "Measurement of the refractive index of distilled water from the near-infrared region to the ultraviolet region," *Appl. Opt.* **46**(18), 3811–3820 (2007).
46. D. Arifler et al., "Light scattering from collagen fiber networks: micro-optical properties of normal and neoplastic stroma," *Biophys. J.* **92**(9), 3260–3274 (2007).
47. V. Ottani et al., "Collagen fibril arrangement and size distribution in monkey oral mucosa," *J. Anat.* **192**, 321–328 (1998).
48. E. Cone-Kimball et al., "Scleral structural alterations associated with chronic experimental intraocular pressure elevations in mice," *Mol. Vision* **19**, 2023–2039 (2013).
49. Z.-H. Zhou et al., "Reorganized collagen in the tumor microenvironment of gastric cancer and its association with prognosis," *J. Cancer* **8**(8), 1466–1476 (2017).
50. A. Devendra et al., "Histochemical analysis of collagen reorganization at the invasive front of oral squamous cell carcinoma tumors," *J. Invest. Clin. Dent.* **9**(1), e12283 (2018).
51. C. J. Hanley et al., "A subset of myofibroblastic cancer-associated fibroblasts regulate collagen fiber elongations which is prognostic in multiple cancers," *Oncotarget* **7**(5) 6159–6174 (2016).
52. S. L. Jacques, "Optical properties of biological tissues: a review," *Phys. Med. Biol.* **58**(11), R37–R61 (2013).
53. R. Samatham, K. G. Phillips, and S. L. Jacques, "Assessment of optical clearing agents using reflectance-mode confocal scanning laser microscopy," *J. Innovative Opt. Health Sci.* **3**(3), 183–188 (2010).

**Isa Carneiro** received her BSc degree in pathological anatomy from Porto Polytechnic Institute in 2008 and her MSc degree in oncology from Porto University in 2012. She is a technician of pathological anatomy at the Department of Pathology of Portuguese Oncology Institute of Porto and is also a member of Cancer Biology and Epigenetics Group of Portuguese Oncology Institute of Porto Research Center. Her main research focus at the present is prostate cancer.

**Sónia Carvalho** is currently a fourth-year pathology resident at Portuguese Oncology Institute of Porto. She received her MD degree from the Faculty of Medicine of Coimbra University, Portugal, in 2012. In January 2013, she started supervised medical practice at Centro Hospitalar Lisboa Norte, Portugal. She participates in different medical and scientific activities within the scope of the residency. Her main research focus, at present, is colorectal carcinoma. She is a member of European Society of Pathology.

**Vânia Silva** is a senior researcher at CIETI—Polytechnic of Porto, Portugal. She received her MSc degree in chemical engineering—Environmental Protection Technologies from Polytechnic Institute of Porto-School of Engineering, Portugal, in 2011. Currently, she is a PhD student at Porto University. Her main research is focused on leather production, collagen stabilization, and waste valorization.

**Rui Henrique** received his MD and PhD degrees from Abel Salazar Institute of Biomedical Sciences-University of Porto (ICBAS-UP), in 1992 and 2006. He became attending pathologist, subspecialized in hematopathology and uropathology, in 2001, director of Department of Pathology in 2006, and senior researcher of Cancer Biology and Epigenetics Group in 2008 at Portuguese Oncology Institute of Porto, as well as invited full professor of ICBAS-UP. His research is focused on epigenetic alterations as cancer biomarkers in urological cancer.

**Luís Oliveira** is a professor and researcher at CIETI/physics department of the Polytechnic Institute of Porto-School of Engineering, Portugal. He received his PhD in biomedical engineering from

Porto University, Portugal, in 2014. In recent years, he has authored and reviewed several papers in the field of tissue optical clearing. His main research interests are tissue optics, optical clearing and related applications, chemical diffusion in tissues, and optical properties control to develop new clinical methods.

**Valery V. Tuchin** is a professor and head of optics and biophotonics at Saratov State University (National Research University of Russia)

and several other universities. His research interests include tissue optics, laser medicine, tissue optical clearing, and nanobiophotonics. He is a fellow of SPIE and OSA, has been awarded Honored Science worker of Russia, SPIE Educator Award, FiFiPro (Finland), Chime Bell Prize of Hubei Province (China), and Joseph W. Goodman Book Writing Award (OSA/SPIE).